ROTOR-DYNAMIC ANALYSIS OF A TIDAL TURBINE CONSIDERING FLUID STRUCTURE INTERACTION AND YAWED FLOW

ANDRE LAß[1,a], MATTI SCHILLING[1,b] AND FRANK-HENDRIK WURM[1,c]

[1] Institute of Turbomachinery, Department of Mechanical Engineering and Marine Technology,
University of Rostock
Albert-Einstein-Str. 2, 18059 Rostock, Germany

[a] andre.lass@uni-rostock.de, www.itu.uni-rostock.de

[b] matti.schilling@uni-rostock.de

[c] hendrik.wurm@uni-rostock.de

Key words: Rotor dynamics, Bond graphs, Fluid-Structure-Interaction, Unsteady-Vortex-Lattice-Method

Abstract. This Paper deals with the rotor dynamic analysis via bond graphs, bi-directional coupled to an unsteady vortex lattice method solver. Hence, no determination of hydrodynamic coefficients is needed to consider fluid induced loads and added mass effects. The rotor-dynamic behavior of a yawed tidal stream turbine is investigated with varying blade flexibilities.

1 INTRODUCTION

In the design phase for submerged turbomachines rotor dynamic analysis is mandatory to ensure stability and reliability of the system. Therefore effects alike vibrations due to fluid flow, electric grid fluctuations and manufacturing related eccentricities have to be considered. Additionally fluid-induced reaction forces related to damping and added mass effects are of interest. The prediction of the latter is usually performed using hydrodynamic coefficients gained in experimental investigations, from empirical formulas or computational fluid dynamic methods.

In this work a time resolved dynamic solution is conducted for the complete power train. It's electro-magnetic and multi body dynamics solution is coupled to a computational fluid dynamics method. This results in a straightforward rotor dynamic analysis including bi-directional fluid-structure-interaction coupling (FSI) to overcome hydrodynamic coefficients determination.

As a typical submersed turbomachine a tidal turbine is investigated in this work. The electromagnetic and structural dynamics are modeled using the bond graphs methodology

(BG). In the fluid domain water is modeled as incompressible inviscid fluid and potential theory is applied via an unsteady vortex lattice method (UVLM) to calculate the fluid-induced forces.

BG is a suitable approach to create models of a complex dynamic system considering the interaction of several energy domains. Due to the energy based nature of the basic modeling elements and the graphical representation of the system dynamics the method generally provides more physical insights towards the rotor-dynamic phenomena from an energy flow and visual perspective [1]. Using BG for rotor-dynamic analysis was studied by [2] with limitation to simple models and structural domain only. Sanchez and Medina [3] created a more detailed BG model for a wind turbine and analyzed its power output behavior including structural dynamics except rotor-dynamics. Another investigation of tidal turbine rotor dynamics using BG was conducted by Laß et. al [6] studying the influences of shear stream profiles and water waves on the orbital displacements of the drive train in the rotor disc.

The UVLM for rotatory devices originates from Kerwin [4] who first introduced a lifting surface method based on vortex ring elements for ship propellers under steady state conditions. For unsteady conditions the method was further developed by [5]. The in-house implemented UVLM-code has been verified in [6] and is compared against flow conditions [7] for 0° and 30° yawed flow conditions here.

In this work additional degrees of freedom regarding the rotor blades are considered within the BG system model and the coupled UVLM referring to [6]. Two sets of simulation series are conducted considering bidirectional FSI for three sets of linear-elastic blade properties (nearly rigid to highly flexible) respectively. First, stationary, uniform inflow conditions are applied, to derive performance curves. Second, a yaw flow angle is set to simulate fluid-induced thrust and torque. The frequency spectra of orbital displacement paths are compared in order to investigate the effects of flexible blades on the rotor dynamic behavior. Hereby, the applicability and effectiveness of the conducted Fluid-Structure-Interaction and multi-physic modeling approach is shown. For the further use this approach results in a parametric dynamic system model for a wide spread of applications like wind and water turbines, submersible mixers and ship propellers.

2 BOND GRAPHS

Bond graphs provide a platform to model power exchange, energy dissipation and storage in a dynamic system of any physical domain with a unified graphical language. The basic variables in bond graphs are effort (e), flow (f), time integral of effort (p) and time integral of flow (q). Effort & flow for electrical and structural system are voltage & current and force & velocity respectively. These variables are transferred throughout the system components via power bonds, preserving the power, defined as the product of effort and flow. Junctions define the constraint structure of a system. When power bonds are joined at a 1-junction, this relates to equal flows at all connected bonds, while efforts sum up to zero. On the contrary, if they are joined at a 0-junction, efforts are equal at all connected bonds, while flows sum up to zero. The constraint structure connects all

bond graph elements based on their preferred causality and energy behavior. The basic single port elements are source of effort (**SE**), source of flow (**SF**), inertial (**I**), compliant (**C**) and resistive (**R**) elements. These elements add, store or dissipated power within the system. Basic two-port elements are transformers (**TF**) and gyrators (**GY**), which are used for power transformation processes.

An algorithmic procedure is applied to the bond graph of an interacting dynamic system, which leads to the equations of motion. Hereby, the following generalized system equation is determined, where X is the state vector, U is the input vector, A is the system matrix and B is the input matrix:

$$\frac{\partial}{\partial t}\{X\} = [A]\{X\} + [B]\{U\} \ . \tag{1}$$

Bond Graphs can be used to model physical effects on a component or sub-model level. By combining these sub models, even for a complex system the equations of motion can be derived and solved with ease.

2.1 system model of the tidal turbine and its power train

In Fig. 1 the system model of the idealized tidal turbine power train is shown. The derived component based bond graph model of this power train is shown in Fig. 2. This is a parametric and generic model, which can be utilized for any size of horizontal axis turbines to predict life and real-time behavior at various boundary conditions. Theoretical informations about the bond graph sub-models used for the Low-speed Shaft, Gearbox, ball bearings and Induction Machine can be found in Lass et. al [6].
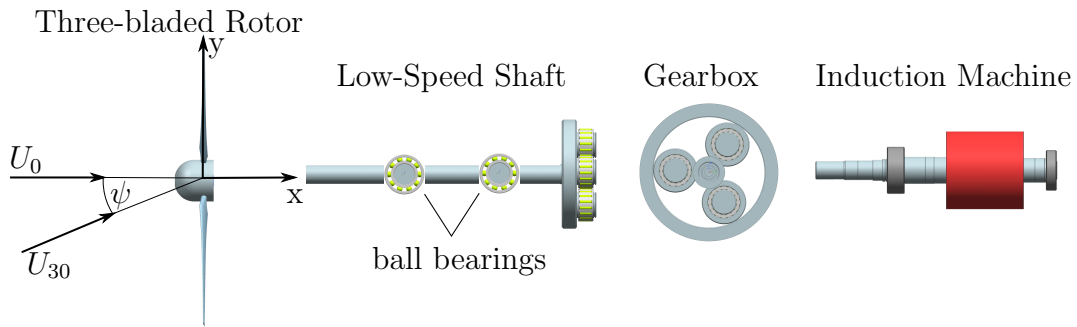
Figure 1: idealized power train of horizontal axis tidal turbine
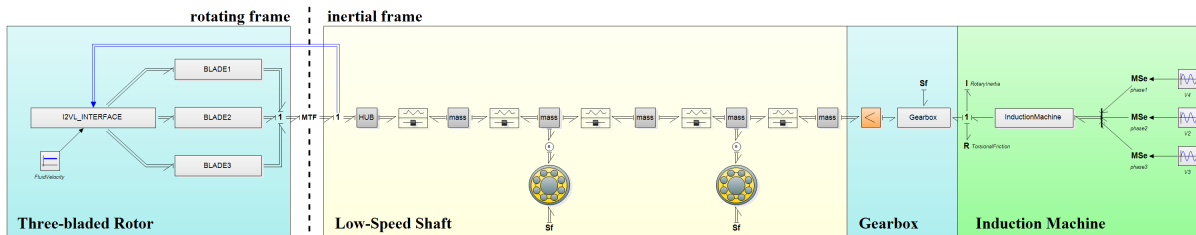
Figure 2: Representation of tidal turbine power train using bond graph based components

The focus of this effort is the integration of a bi-directional fluid-structure interaction, which considers axial and tangential rotor blade displacements in rotor dynamic analyzes. Below, the bond graph model of a three-bladed rotor will be briefly described.

2.2 Three-bladed Rotor

The Three-bladed Rotor consist of two sub models. First, a single sub model for the blades, which differs in the initial positions of each blade section masses. Second, a equation based coupling sub model, which interfaces between the unsteady vortex lattice code implemented in Matlab for hydrodynamic load calculations and the bond graph model in 20sim for structural dynamic analysis. The implemented coupling scheme will be explained in section 5.

At the rotor blades three translational (x, y, z) and three rotational (φ, θ, ψ) degrees of freedom are considered, relating to axial, horizontal and vertical directions and associated rotations, respectively. All blades are modeled in the body fixed rotating frame of the hub. As the blade roots are attached to the hub and share the same flow, while their loads sum up, a **1**-junction is used to connect them via BG to the Low-Speed-Shaft. Each blade is discretized as a flexible structure using four 3D beam elements with lumped mass properties (Fig. 3 upper box). A rigidly moving reference frame is defined to determine the relative local flows of each beam node (Fig. 3 middle box). Using **0**-junctions, relative flow differences are derived. Via the combine & share module, these flows are combined and transmitted towards the coupling sub model, while in the opposite direction the hydrodynamic loads are distributed (Fig. 3 lower box). The relative displacements of each blade section used for bidirectional FSI are calculated by integrating the flow differences with respect to time.
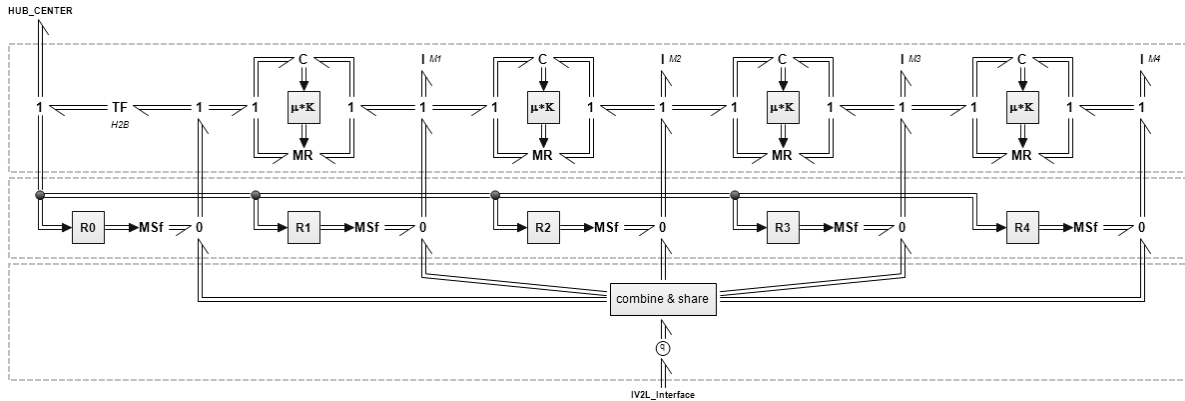
Figure 3: Bond Graph model of single Blade

Within the compliant elements (**C**) a common 12×12 stiffness matrix K_R is defined in the rotor coordinate system, which results from transforming the local stiffness matrix of each 3D-beam element in the blade coordinate frame by its Cardan angles:

$$K_R = T_l^T K_l T_l \tag{2}$$

4

Here T_l represents the local transformation matrix. The modulus of the resistive element (MR), relates to the internal Rayleigh damping with the modulus m:

$$m = \mu \cdot K_R \quad, \text{ with: } \quad \mu = 2.5 \cdot 10^{-5} \;. \tag{3}$$

The inertial properties of the blades section centers are defined relative to the rotor coordinate system using a 6×6 Inertial element ($\mathbf{I}$).

3 UNSTEADY VORTEX LATTICE METHOD

The UVLM is based on potential theory, hence, water is modeled as incompressible, irrotational and inviscid fluid except for the discontinuity surfaces. These surfaces generally are modeled by a distribution potential Φ. As the definition of Φ for a vortex ring element is complex, Röttgermann et. al [5] and Katz and Plotkin [8] have shown the equivalence of the velocity $\nabla\Phi$ induced by a vortex ring element enclosing the same surface as a dipole element. Based on this the chosen formulation for $\nabla\Phi$ in Eq. (4) results from N quadrilateral vortex rings.

$$\nabla\Phi = \frac{1}{4\pi} \sum_{i=1}^{N} \sum_{j=1}^{4} \frac{r_{1ij} \times r_{2ij}}{|r_{1ij} \times r_{2ij}|^2} \left(\frac{r_{0ij} \cdot r_{1ij}}{|r_{1ij}|} - \frac{r_{0ij} \cdot r_{2ij}}{|r_{2ij}|} \right) \Gamma_i \tag{4}$$

Hereby Γ_i is the constant vortex strength of a quadrilateral vortex ring. r_0 is the vector along a straight vortex filament, whereas r_1 and r_2 represent vectors between the point P and the vortex filament start and end points.

The total velocity U_P in P can be found by superposition of induced velocities and free stream velocity U_∞ as illustrated in Eq. (5).

$$U_P = \underbrace{\nabla\phi_W}_{\text{turbine blade(s)}} + \underbrace{\nabla\phi_{VS}}_{\text{free vortex sheet(s)}} + \underbrace{U_\infty}_{\text{free stream velocity}} \tag{5}$$

A set of N vortex rings leads to a linear system $\sum_i^N a_{ik}\Gamma_i = R_k$, where Γ_i represents the current circulation in vortex ring element i. The right hand side $R_k = U_k$ consists of the velocity components in the kth arbitrary point P.

a_{ik} is an element of the geometrical related influence matrix, which equates the amount of velocity induced by the vortex ring i onto the kth collocation point, if a circulation $\Gamma_i = 1$ is assumed. If the geometry changes over time the influence matrix changes as well. In the presented work it is recalculated in every time step due to blade deformations and wake convection.

$$a_{ik} = \frac{1}{4\pi} \cdot \sum_{j=1}^{4} \frac{r_{1ij} \times r_{2ij}}{|r_{1ij} \times r_{2ij}|^2 + |r_{sij}|^2} \left(\frac{r_{0ij} \cdot r_{1ij}}{|r_{1ij}|} - \frac{r_{0ij} \cdot r_{2ij}}{|r_{2ij}|} \right) \tag{6}$$

Desingularization is performed following Ramseys [9] formulation $|r_{sij}| = \delta_i |r_{oij}|$ which relates to the vortex filament length and applies a viscous vortex core behavior $\delta_i =$

$\sqrt{4\nu_{kin}t_i}$ with kinematic viscosity ν_{kin} and elapsed time t_i since the vortex ring i shed from the trailing edge.

In the presented implementation the quadrilateral vortex ring elements are located at the camber surface. In span wise direction a half cosine spacing is applied with refinement at the blade tip while in chord wise direction an equidistant distribution is chosen. Following the lumped vortex theory the ring elements are shifted in chord wise direction about 1/4th of a vortex ring length towards the trailing edge. The collocation points are located in the center of the ring elements. [8]

Kelvins theorem is satisfied by a wake vortex lattice of vortex rings shedding from the lifting surface. It is implemented force free where the wake propagates with the total velocity U at the edges of the vortex ring elements. The required vortex strength of the first wake panel strip is equal to the vortex strength of the blades vortex rings shed at the trailing edge in the previous time step and is held constant for the vortex ring element during the calculation. [10]

The potential theory force vector F_{pot} results from the unsteady Kutta-Joukowski theorem following [11]:

$$F_{pot_{ik}} = \rho_{fl}\left[U_{ik} \times \Delta l_{ik}\Gamma_{\Delta l_{ik}} + \left(\frac{\Delta\Gamma_{ik}}{\Delta t}S_{ik}\right)n_{ik}\right].\tag{7}$$

Here, the indices i and k denote the radial and chordwise panel position, respectively. ρ_{fl} is the density of the fluid, Δl_{ik} is the vector of vortex filament lengths, Δt represents the time step size and S_{ik} is the panel surface. $\Gamma_{\Delta l_{ik}}$ represents the bound circulation on Δl_{ik}. For the leading edge vortex filaments it is equal to Γ_{ik}, while for any other filament it is defined as the difference of circulation between two neighboring panels in chordwise direction. The second term on the right hand side of Eq. (7) refers to the added mass effect of the surrounding fluid. Suction forces at the leading edge and frictional effects have been considered as described in Lass et. al [6].

4 MAPPING SCHEME

The implemented mapping algorithm ΔGRID uses a linear interpolation, extrapolation and distribution scheme. It is visualized in Fig. 4. Two cases are distinguished: (a) a grid node point k between the mass points j and $j + 1$; (b) for a node k near to the blade tip beyond the last mass point $j + 1$. In both cases the interpolation, extrapolation and distribution refer to the distance $\vec{s}$ normal to the mass point plane. This plane is defined perpendicular to the beam axis in the mass point.

In (a) the distribution of force $\vec{F}$ and interpolation of displacement $\vec{X}$ is performed as follows:

$$\vec{F}_{k,j} = \vec{F}_k \cdot \frac{|\vec{s}_{k,j+1}|}{|\vec{s}_{k,j}| + |\vec{s}_{k,j+1}|} \qquad \vec{X}_{k,j} = \vec{X}_j \cdot \frac{|\vec{s}_{k+1,j}|}{|\vec{s}_{k,j}| + |\vec{s}_{k+1,j}|}$$

$$\vec{F}_{k,j+1} = \vec{F}_k \cdot \frac{|\vec{s}_{k,j}|}{|\vec{s}_{k,j}| + |\vec{s}_{k,j+1}|} \qquad \vec{X}_{k,j+1} = \vec{X}_{j+1} \cdot \frac{|\vec{s}_{k,j}|}{|\vec{s}_{k,j}| + |\vec{s}_{k+1,j}|} \tag{8}$$

In case (b) $\vec{F}$ is transferred completely onto node $j+1$ while $\vec{X}$ is extrapolated from the two closest mass points.

$$\vec{F}_{k,j} = \vec{F}_k \qquad\qquad \vec{X}_k = \vec{X}_{j+1} + (\vec{X}_j + \vec{X}_{j+1}) \cdot \frac{|\vec{s}_{k+1,j}|}{|\vec{s}_{k,j}| + |\vec{s}_{k+1,j}|} \qquad (9)$$

The described procedure is performed for every grid node and its adjacent mass points so that the total forces onto one mass point result from the sum over all node points in the adjacent Blade sections.
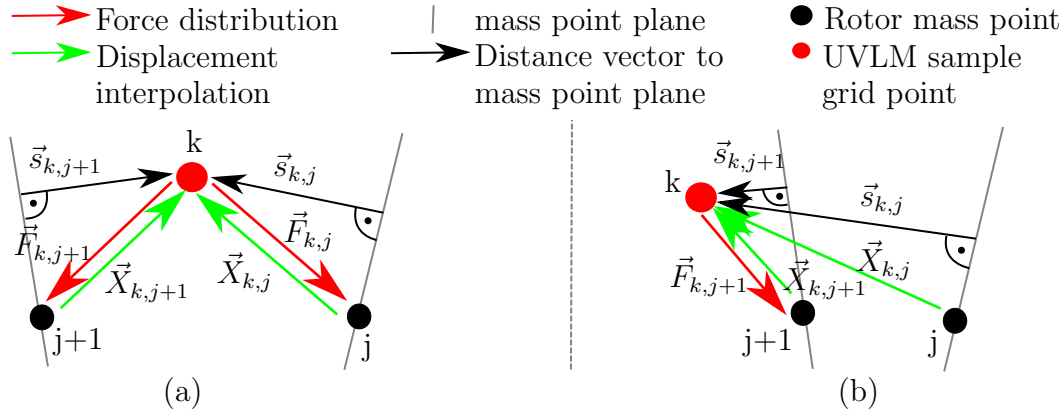
Figure 4: schematic FSI mapping visualisation for (a) a node between two mass points and (b) a node at the blade tip

5 FSI-COUPLING METHOD

On the One hand, a multi-step implicit backward differential formula solver is used to solve the equations of motions derived using the bond graph models in 20sim. On the other hand, I2VL is based on an explicit time-stepping algorithm with a constant macro time step width Δt_{I2VL}.
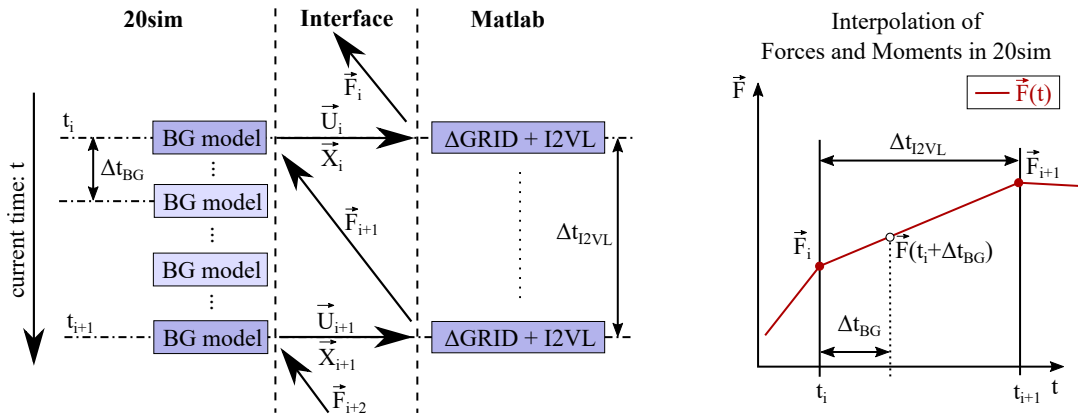
Figure 5: schematic overview for FSI coupling

7

In Fig. 5 the coupling scheme between the involved solvers is visualized. At each macro time t_i 20sim transmits the current velocities and displacements of the Hub (inertial frame) and blades (body fixed frame) to I2VL. I2VL then linearly extrapolates/ interpolates the blade displacements of the 20sim beam nodes at the corresponding vortex lattice grid points based on their node distance along the beam section axis as presented in section 4. As I2VL is executed it advances in time by Δt_{I2VL} and determines the fluid loads on each collocation point at the subsequent macro time t_{i+1} . Via mapping scheme the associated loads at the blade beam nodes $\vec{F}_{i+1}$ are derived and transmitted to 20sim. 20sim advances and integrates the state variables with respect to time, while the current loads at time t are linearly interpolated using the previous loads $\vec{F}_i$ and the next loads $\vec{F}_{i+1}$:

$$\vec{F}(t) = \vec{F}_i + \frac{\vec{F}_{i+1} - \vec{F}_i}{\Delta t_{I2VL}}(t - t_i) \tag{10}$$

The following limitations of presented FSI-approach are to be named:

- Load dependent passive pitch of the blade/beam axis is not considered yet.

- No shortening of beam along its axis due to large deflections is modelled.

- A damping coefficient of 0.2 Ns/m is assumed for blade beam nodes moving relative to the rigid rotor reference frame.

6 TEST CASES

The test case setup consists of the investigation of dynamic drive train behavior and the blade displacements of a 30° yawed tidal turbine in undisturbed fluid flow field. The turbine geometry has been derived from Bahaj et al. [7], with a defined blade pitch angle of 25°. Low-speed-shaft, ball bearing, planetary gearbox and induction machine parameters can be found in Laß et. al [6]. Input parameters for the blade can be given on request. The BG model of the tidal turbine power train with bi-directional FSI coupling is simulated for three different blade materials. The materials have been chosen in order to investigate the influence of blade deflections on the rotor orbital displacements. The materials cover a range from nearly rigid to flexible blade behavior. The following materials have been selected: steel (nearly rigid), aluminum and composite (flexible). Composite refers to an arbitrary material with comparatively small Youngs modulus and density. The basic material properties for the three materials used in this work are given in Tab. 1.

Table 1: Material Properties

Parameter	Steel	Aluminium	Composite
Young's modulus E / [GPa]	210	71	18.5
Poisson's ratio ν / [-]	0.3	0.33	0.31
Density ρ / [kg/m^3]	7850	2770	1010

As mass eccentricity is not investigated here, the lateral low-speed shaft displacements are mainly effected by hydrodynamic forces and moments acting perpendicular to the rotor

axis. Therefore, a 30° yaw angle ψ for the fluid inflow towards the rotor is investigated (cf. Fig. 1).

7 VERIFICATION

The dynamic behavior of the structural power train components in the bond graph model have been verified by comparing natural frequencies and displacements with higher order FEM-Simulations conducted in Ansys Mechanical. The natural frequencies of the bond graph model have been determined by imparting an impulse in terms of an initial momentum to one or more components. As a result, in a system with reduced damping the masses are vibrating with their natural frequencies, which can be extracted using a Fast-Fourier-Transformation (FFT) on the derived velocity- or displacement-time signals. The determined natural frequencies of a single blade in a fluid-free environment are given in Tab. 2. The first and second eigen-frequencies of the blade relate to out-of-plane modes and are in good agreement with FEM-results. The largest deviations are observed in the third mode (mixed in-/out-of-plane). 4th and 5th eigenmodes (out-of-plane) have also been detected with differences less than 10%. The difference between the bond graph and

Table 2: Comparison of blade natural frequencies

material	Steel			Aluminum			Composite		
mode	1	2	3	1	2	3	1	2	3
Ansys Mechanical	100	322	484	101	323	486	85	273	410
Impact Test BG Model	100	320	420	99	308	413	83	261	348

FEM-results is less than 2% for the first three modes. Besides the natural frequencies the displacements of a single blade loaded at the tip with 10 N in axial direction have been compared. The difference of resulting axial tip displacements was found to be less than 3.6% for all material sets.
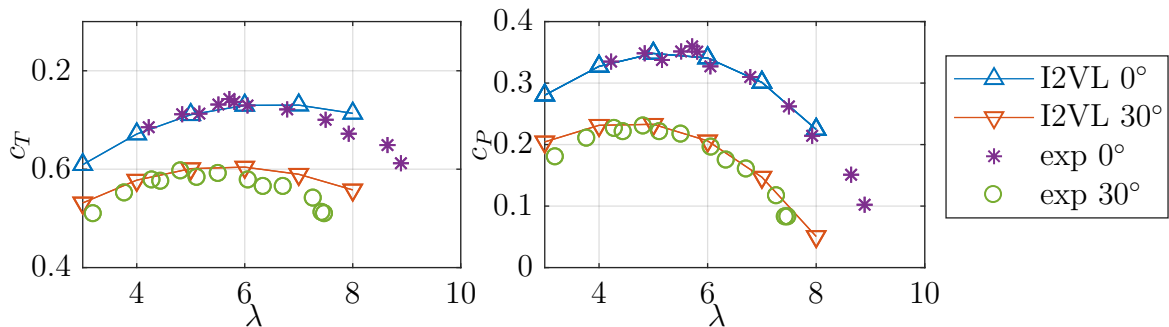
Figure 6: Power and Thrust curves from I2VL compared to experimental Data from [7]

A uniform inflow velocity distribution has been assumed for all simulations. For inflow yaw angles ψ of about 0° and 30° the integral hydrodynamic loads determined by the I2VL code are validated against experimental results from [7]. The results shown in

Fig. 6 reveal a good agreement of thrust and power coefficients (c_T, c_p) at various tip speed ratios λ. Best match is found at $\lambda = 6$, therefore it has been chosen for the rotor-dynamic simulations, with the undisturbed inflow speed: $U_\infty = 1.8$ m/s $(n \approx 255$ RPM$)$.

8 RESULTS

The axial displacements of a single blade for $0°$ and $30°$ yaw inflow angle considering the presented bi-directional FSI approach are shown in Fig. 7. For $0°$ inflow angle the axial displacements of the blades converge to a constant value over time, while for $30°$ it is a function of the current angular position. The range of axial displacements for $30°$ yaw is indicated by a gray background in Fig. 7. For a nearly rigid blade the range is very small, while along With an increasing structural flexibility the range of axial displacement over a complete revolution increases.
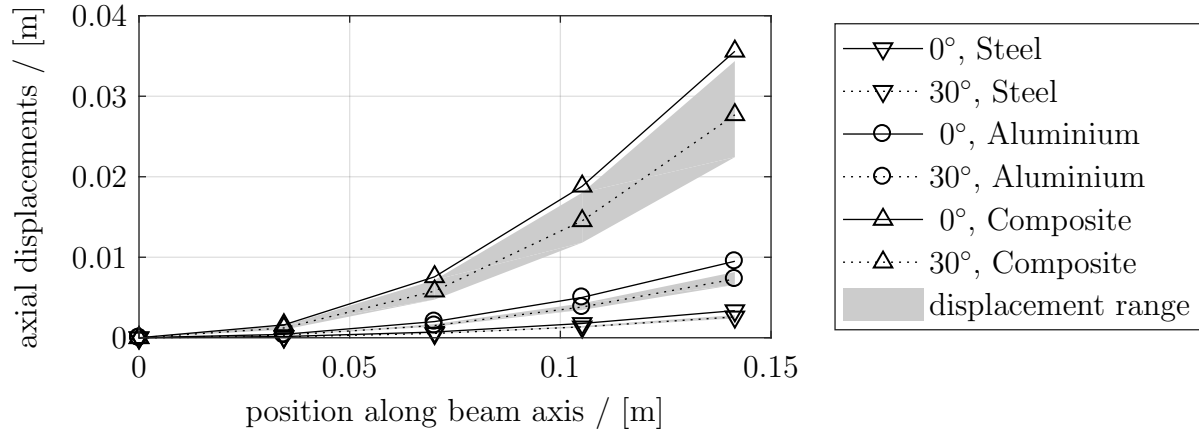
Figure 7: Axial blade displacements of a single blade considering the presented bi-directional FSI approach

The varying range of blade displacements due to bi-directional FSI adds thrust on a single blade over one revolution. To investigate this influence a thrust coefficient $C_{T,b}$ of a single blade b is defined as:

$$C_{T,b} = \frac{T_b}{\frac{1}{2}\rho U_\infty^2 A} \tag{11}$$

Where T_b and A refers to the blade thrust and rotor area respectively. In Fig. 8 (a) the blade thrust coefficient is plotted based on the blades angular position in the y,z-rotor plane viewed from the non-rotating inertial frame. Here, the yawed inflow is heading towards the viewer from left to right. When the blade is located upstream (left side), towards the yawed inflow, it is observing a higher thrust compared to its downstream location (right side). As a result, the blade will have higher displacements with increasing flexibility at an upstream location. At the downstream location axial displacements and thrusts are decreased. Both observations can be explained considering the distance

of a blade towards the shed wake field of the rotor, which is convected downstream. In the turbine case the decreased distance at the downstream region correlates to a reduced circulation and subsequently to a reduced thrust of the passing blade. This effect is further amplified with increasing structural flexibility as shown in Fig. 8 (a). The presented bi-directional FSI approach has only negligible effect on the total amount of rotor thrust because passive blade pitching is not considered. But the eccentricity of the thrust application point increases proportional with the blade flexibility.

The unequal thrust distribution of the blades is causing bending moments acting on the rotor hub. In the non-rotating inertial frame the effect of flexibility and increased unequal thrust distribution can be observed in terms of the orbital paths of the rotor center.
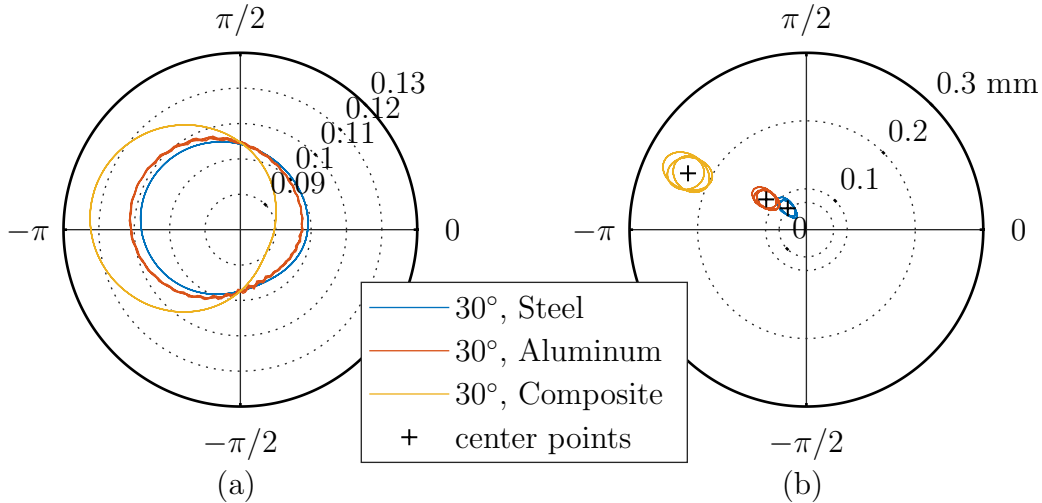
Figure 8: Comparison of (a) single blade thrust coefficients and (b) orbital hub paths based on angular position in y-z rotor plane for 30° yaw inflow

Fig.8 (b) visualizes the orbital path of the hub in the rotor plane. With increasing blade flexibility the orbital path center is moving northwest following the growing thrust imbalance. It can be inferred, that a turbine rotor tends to aligning with the inflow direction and higher blade flexibilities will contribute to this.

In Fig. 9 the frequency spectra of the hub radial displacements are shown. As the turbine is operating at about 255 revolutions per minute the excitation or operating frequency f_o is about 4.25 Hz. This peak can be observed for all blade materials. Then due to the number of blades $N_b = 3$ a blade passing frequency $f_b = f_0 N_b$ at about 12.75 Hz is expected which can be clearly identified.

With increasing flexibility the second order of f_0 is amplified, which implies, that super-synchronous excitation frequencies may occur, which shall be considered in the early development phase.
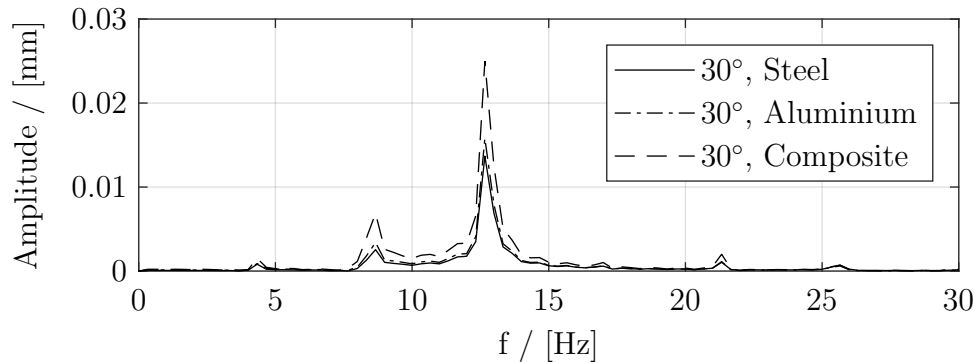
Figure 9: Frequency spectra of hub displacements in Y-direction

9 CONCLUSIONS

Within this paper an approach towards modeling the rotor-dynamic behavior of a tidal turbine incorporating bi-directional Fluid-Structure-Interaction is presented.

It is shown that the presented method is capable to meet the natural frequencies calculated by higher order methods regarding operation and passing frequencies. The results suggest that the thrust eccentricity and super-synchronous excitation frequencies are amplified due to raised blade flexibility.

REFERENCES

[1] Pedersen, E. Rotordynamics and bond graphs: basic models *Mathematical and Computer Modelling of Dynamical Systems* (2009) **15(4)**:337-352.

[2] Campos, J., Crawford, M., Lane, W. B. and Longoria, R. Rotordynamic Modeling Using Bond Graphs: Modeling the Jeffcott Rotor, *IEEE* (2004) **41(1)**: 274–280.

[3] Sanchez, R. and Medina, A. Wind turbine model simulation: A bond graph approach, *Simulation Model. Pract. Theory* (2014) **41**:24–45.

[4] Kerwin, J. E., Lee, C. S. Prediction of steady and unsteady marine propeller performance by numerical lifting-surface theory, *SNAME - The Society of Naval Architects and marine Engineers* (1978) **86(8)**: 218-253.

[5] Röttgermann, A., Behr, R., Schöttl, Ch. and Wagner, S. Calculation of Blade-Vortex Interaction of Rotary Wings in Incompressible Flow by an Unsteady Vortex-Lattice Method Including Free Wake Analysis *Numerical techniques for boundary element* (1992) **33(7)**:153–166.

[6] Laß, A., Schilling, M., Kumar, J. and Wurm, F.-H. Rotor dynamic analysis of a tidal turbine considering fluidstructure interaction under shear flow and waves. *International Journal of Naval Architecture and Ocean Engineering* (2018), https://doi.org/10.1016/j.ijnaoe.2018.03.002.

[7] Bahaj, A. S., Molland, A. F., Chaplin, J. R. and Batten, W. M. J. Power and thrust measurements of marine current turbines under various hydrodynamic flow conditions in a cavitation tunnel and a towing tank, *Renewable Energy* (2007) **32(3)**:407–462.

[8] Katz, J. and Plotkin, A. *Low speed Aerodynamics: From Wing Theory to Panel Methods*, ser. Aeronautical and Aerospace Engineering. USA: New York: McGraw-Hill, 1st Edition, 1991.

[9] Ramsey, W. D. *Boundary Integral Methods for Lifting Bodies with Vortex Wakes*, Dissertation, Massachusetts Institute of Technology, Department of Ocean Engineering, 1996.

[10] Burger, C. *Propeller performance analysis and multidisciplinary optimization using a genetic algorithm*, Dissertation, Auburn University, Aerospace Engineering Department, Auburn, Alabama, 2007.

[11] Pesmajoglou, S. P. and Graham, J. M. R. Prediction of aerodynamic forces on horizontal axis wind turbines in free yaw and turbulence, *Journal of Wind Engineering and Industrial Aerodynamics* (2000) **86**:1-14.